Impact of a viscous drop on a superhydrophobic surface and evolution to a pyramid

By YURIKO RENARDY[1], STÉPHANE POPINET[2], LAURENT DUCHEMIN[3], MICHAEL RENARDY[1], MARY ANN CLARKE[1], STÉPHANE ZALESKI[3] AND CHRISTOPHE JOSSERAND[3]

[1]Department of Mathematics and ICAM, 460 McBryde Hall, Virginia Tech, Blacksburg, VA 24061-0123, USA

[2]National Institute for Water and Atmospheric Research, PO Box 14 901, Kilbirnie, Wellington, New Zealand

[3]Modélisation en Mécanique, CNRS-UMR 7607, Université Pierre et Marie Curie, 8 rue du Capitaine Scott, 75015 Paris Cedex 05, France

When a drop of clean water impacts a superhydrophobic surface, the liquid is forced to spread out due to inertia. Once a maximum radius is attained, the liquid retracts and finally bounces back off the surface. Some of the kinetic energy is stored as surface energy and generates capillary waves which travel from the bottom of the impacted drop towards the top. This results in the evolution of the drop to a pyramid. These features have recently been experimentally recorded by Richard (2000). In the experiments, the maximal spreading of the drop did not entirely balance the loss of kinetic energy. Thus, the question arose: what accounts for this remaining kinetic energy?

In this paper, numerical simulations are performed with an axisymmetric volume-of-fluid method treating the coupled two-fluid water/air system in full, and secondly with an axisymmetric front-tracking algorithm treating the water/air system as a free surface problem. It is found that the two methods retrieve qualitatively similar results. Computations of the kinetic energy, velocity field, pressure field, and interface evolution are presented. It is shown that when the kinetic energy is at the first minimum value, the drop has spread to its maximal radius. However, there is stored kinetic energy in the form of a vortical swirling motion which persists in the toroidal drop. The center almost dries, and thereafter, the drop begins its bounce upwards. The velocity field is primarily upwards at this stage, as the central region rises, followed by the surrounding toroidal region. The drop then leaves the ground and rises, achieving a top-heavy champignon shape. In these final stages, the kinetic energy is a small fraction of its initial value.

1. Introduction

There are a number of super-hydrophobic surfaces which occur naturally (cf. extensive discussion in Richard (2000); Richard & Quéré (2000); Quéré *et al.* (2000)). An example is the gingko biloba tree, which is used in urban areas for its capacity to resist pollution. The microscopic structure of the leaf is fibrous and aerated. The fibres are coated with a naturally hydrophobic wax. When a water drop impacts it, there is air under the entire

drop between the points of solid-liquid contact. Synthetic surfaces with these properties have also been manufactured. The impact of a drop of clean water against a super-hydrophobic surface results in a pyramid structure, which has been documented in the thesis of Richard (2000). We reproduce the sequence of photographs in figure 1 and quote the description. The timings are 2.7 ms (between photo 1 & 2), 1.8 (between 2 & 3, and so on), 0.4, 1.0, 0.2, 0.2, 0.4, 0.4, and 0.9.

The drop is generated by dripping, and as it falls, it oscillates: the initial shape may be ellipsoidal or an oscillation of mode 2 (Popinet (2000)) in this particular experiment. However, when the experiment was repeated, the initial shape was not always the same. The impact against the solid surface creates waves at the surface of the drop which travel up to the summit. The analogy is that of a pebble thrown into a round pond: the emitted concentric waves go away and meet at a diametrically opposite point, which in this case is the top of the drop. The wavelength which is amplified the most is that with a phase speed equal to the impact speed. It is observed experimentally that the layers have nearly the same height. The wavelength corresponding to the speed V is (cf. Equation (V.16) of Richard (2000))

$$\lambda = \frac{\gamma}{\rho V^2}, \tag{1.1}$$

where γ is surface tension and ρ is density of the viscous drop. For the parameters in figure 1, $V = 40$ cm.s^{-1}, $\gamma = 72.8$ dyn.cm^{-1} at 20 deg.C, $\rho = 1$ g.cm^{-3}, and thus, $\lambda = 0.5$ mm, which is roughly the height of the layers in the figure. The layers collapse, one into the other, and eventually eject a secondary jet. The jet is not always present; when it occurs, it is due to the breaking of capillary waves when they reach the top of the pyramid. The nipple at the top inertially turns over, which generates a small cavity of air at the center of the drop of the size of the nipple. Thereafter, this cavity collapses, emitting the jet. This is reminiscent of simulations of a gas bubble bursting at a free surface (Boulton-Stone & Blake (1993); Popinet & Zaleski (2001); Duchemin *et al.* (2001); Oguz (1998)).

In the sequence of photographs, the center of the drop does not dry out. However, drying out has been observed in instances, when the impact speed is higher.

There is a threshhold for the phenomenon to occur. The excited wavelength must be much smaller than the radius R of the drop, which means that V should be sufficiently large. This condition, that $\lambda < R$, yields the condition on the Weber number:

$$We > 1, \qquad We = \frac{\rho V^2 R}{\gamma}. \tag{1.2}$$

In the case of figure 1, $We \approx 4$. The limiting case of $We = 1$ gives the velocity to be $V = 20$ cm.s^{-1}, and the number of layers is comparable to the value of the Weber number. The capillary waves must reach the top of the drop. These, however, decay over a distance much shorter than the wavelength. The distance ℓ of decay of a wave of wavelength λ propagating at speed V is given by

$$\ell = \frac{\rho \lambda^2 V}{\eta}, \tag{1.3}$$

where η is the viscosity. In order to observe the pyramid structure, this length ℓ must be much larger than the radius of the drop: $\ell > R$. Substituting λ from equation (1.2) into equation (1.3),

$$\frac{\rho R \eta V^3}{\gamma^2} = We.Ca < 1. \tag{1.4}$$

For a drop of radius $R = 0.175$ mm, we have $We.Ca \approx 2 \times 10^{-2}$ and criterion (1.4) is verified. Since this criterion, as well as $We > 1$ must both be satisfied, the window of velocities in which we can observe the liquid pyramid is

$$(\frac{\gamma}{\rho R})^{1/2} < V < (\frac{\gamma^2}{\rho \eta R})^{1/3}. \tag{1.5}$$

For a drop of water of $R \approx 1$ mm, this gives speeds between 26 and 170 cm.s^{-1}. There exists, in particular, a radius R at which this window reduces to one value, but this is of the order of $R = 10^{-6}$ cm, which is much smaller than drops in their experiments. The aim of this paper is the numerical simulation of the formation of the pyramid.

In Section 2, we summarize the two numerical algorithms which we use and the problem formulation. The first, in Section 2.1, is a volume-of-fluid method. This is a two-fluid formulation, in which a volume fraction function is used to reconstruct the interface shape. When the viscosities are small, this formulation suffers from spurious wiggles on the interface, and therefore, the viscosities and densities of the liquids are upscaled in order to perform the simulations. Here, We and $We.Ca$ values from the experiments are used. We show the numerical results in Section 4. The evolution of the kinetic energy is shown and discussed with respective stages in the drop shape.

Secondly, a front-tracking algorithm for a free-surface code is given in Section 2.2. Numerical results are presented in Section 4.

2. Numerical algorithms

2.1. *Volume-of-fluid method: SURFER++*

2.1.1. *Governing equations*

The momentum equations are the axisymmetric Navier-Stokes equations :

$$\rho(\frac{\partial u}{\partial t} + u\frac{\partial u}{\partial u} + v\frac{\partial u}{\partial x}) = -\frac{\partial P}{\partial r} + \frac{1}{r}\frac{\partial(rS_{rr})}{\partial r} + \frac{\partial S_{xr}}{\partial x} - \frac{S_{\theta\theta}}{r} + F_r, \tag{2.1}$$

$$\rho(\frac{\partial v}{\partial t} + u\frac{\partial u}{\partial v} + v\frac{\partial v}{\partial x}) = -\frac{\partial P}{\partial x} + \frac{1}{r}\frac{\partial(rS_{rx})}{\partial r} + \frac{\partial S_{xx}}{\partial x} + \rho g + F_x, \tag{2.2}$$

where $S_{rr} = 2\mu(\partial u/\partial r)$, $S_{\theta\theta} = 2\mu(u/r)$, $S_{xx} = 2\mu(\partial v/\partial x)$, $S_{rx} = \mu(\partial v/\partial r + \partial u/\partial x)$, $S_{xr} = S_{rx} = \mu(\partial v/\partial r + \partial u/\partial x)$, The radial and axial components of velocity are denoted $\mathbf{u} = (u, v)$, and the pressure by P. The body force $\mathbf{F} = (F_r, F_x)$ includes the interfacial tension in the volume-of-fluid formulation. Incompressibility yields:

$$\nabla \cdot \mathbf{u} = \frac{1}{r}\frac{\partial(ru)}{\partial r} + \frac{\partial v}{\partial x} = 0 \tag{2.3}$$

The two fluids are immiscible. Density and viscosity are constant in each phase but may be discontinuous at the interface. We use the VOF scheme. A volume fraction field C is used to represent and track the interface, which is transported by the velocity field $\mathbf{u}$:

$$\frac{\partial C}{\partial t} + \mathbf{u} \cdot \nabla C = 0 \tag{2.4}$$

This equation is used to calculate the density and viscosity. For cells overlying the interface, the average values of density and viscosity are interpolated by the following formulas :

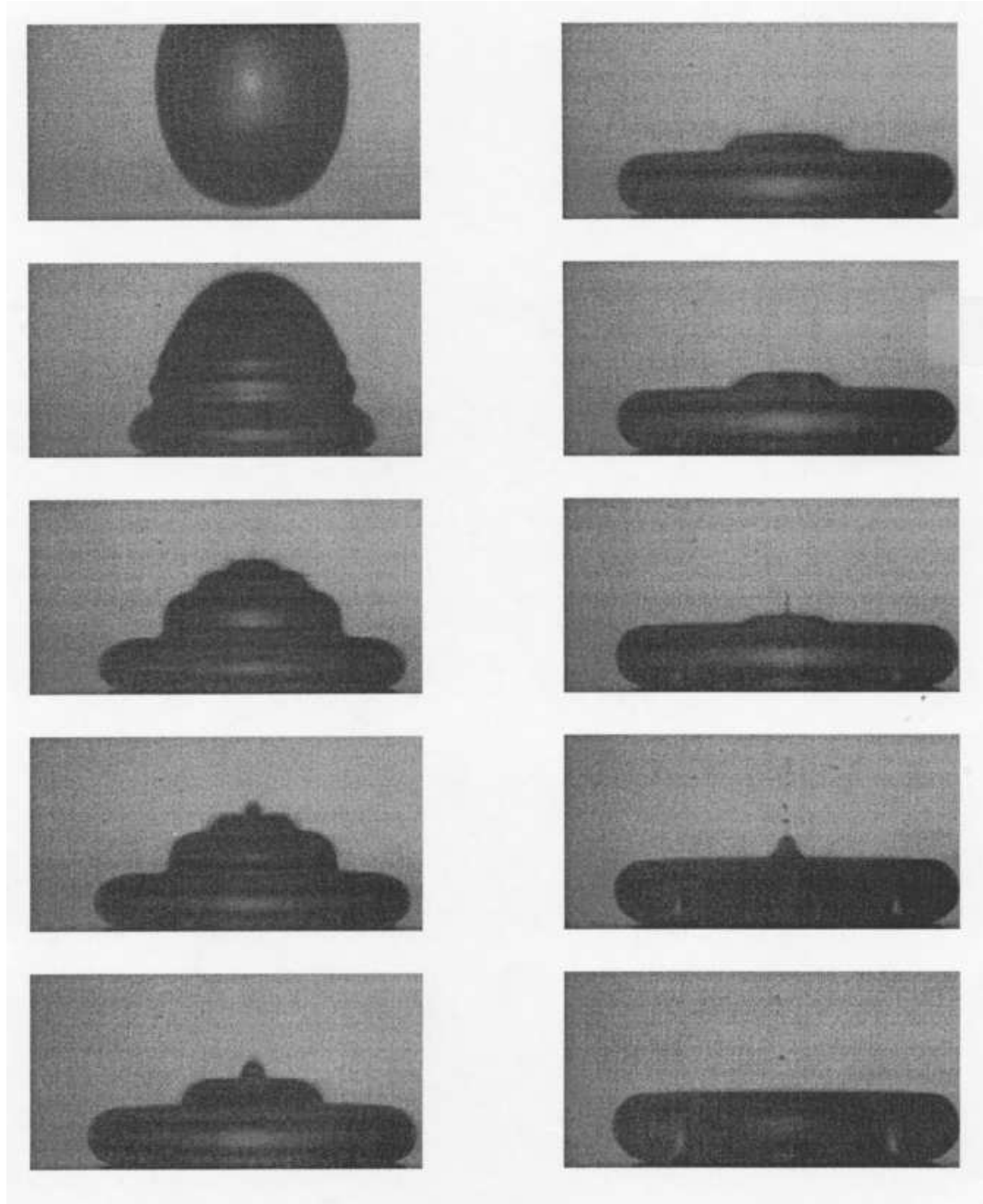$$\rho = C\rho_1 + (1 - C)\rho_2, \qquad \mu = C\mu_1 + (1 - C)\mu_2 \tag{2.5}$$

FIGURE 1. Figure V.15 of Richard (2000). Structures formed during the impact of a drop of radius $R = 1.75$ mm at velocity $V = 41$ cm.s^{-1}. The timings between the frames are 2.7 ms (between photo 1 & 2), 1.8 (between 2 & 3, and so on), 0.4, 1.0, 0.2, 0.2, 0.4, 0.4, and 0.9.

2.1.2. *Discretization*

Our code SURFER++ is composed of three parts: a second order VOF method to track the interface, a projection method to solve the Navier-Stokes equations on the MAC grid, and finally, a continuum method for modeling the interfacial tension. We

(a) (b)
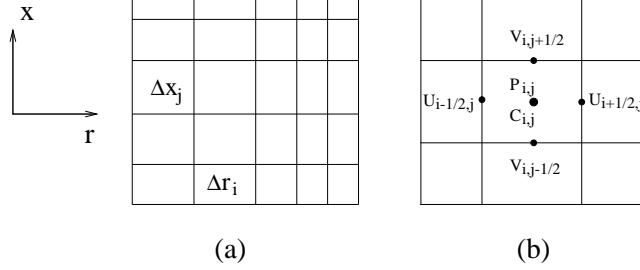
FIGURE 2. (a) Two dimensional Cartesian mesh with variable cell sizes. (b) Location of variables in a MAC mesh cell.

summarize these components below. The axisymmetric code has already successfully simulated fully nonlinear bamboo waves for core-annular flow with high viscosity ratios in Li *et al.* (1998); Renardy & Li (2001). Details of the algorithm are given in Lafaurie *et al.* (1994); Zaleski *et al.* (1995); Gueyffier *et al.* (1999); Li & Renardy (2000). We solve the momentum equations by a projection method. We calculate first an approximate velocity $\mathbf{u}^*$ without the pressure gradient ∇p from the momentum equations, assuming that $\mathbf{u}^n$ is known:

$$\frac{\mathbf{u}^* - \mathbf{u}^n}{\Delta t} = -\mathbf{u}^n \cdot \nabla \mathbf{u}^n + \frac{1}{\rho}(\nabla \cdot (\mu \mathbf{S}) + \mathbf{F} + \rho \mathbf{g})^n. \tag{2.6}$$

In general, the resulting flow field $\mathbf{u}^*$ does not satisfy the continuity equation. However, we require that $\nabla \cdot \mathbf{u}^{n+1} = 0$ and

$$\frac{\mathbf{u}^{n+1} - \mathbf{u}^*}{\Delta t} = -\frac{\nabla p}{\rho}. \tag{2.7}$$

The discretization of of the incompressibility condition (2.3) at cell (i,j) is :

$$\frac{1}{r_i}\frac{r_{i+\frac{1}{2}}u_{i+\frac{1}{2}} - r_{i-\frac{1}{2}}u_{i-\frac{1}{2}}}{\Delta r_i} + \frac{v_{i,j+1/2} - v_{i,j-1/2}}{\Delta x_j} = 0. \tag{2.8}$$

where $r_{i-\frac{1}{2}}$ denotes the left face coordinate of cell (i,j), $r_{i+\frac{1}{2}}$ the right face coordinate and $r_i = \frac{1}{2}(r_{i-\frac{1}{2}} + r_{i+\frac{1}{2}})$. Taking the divergence of Eq. (2.7), we obtain a Poisson-like equation

$$\nabla \cdot \left(\frac{\nabla p}{\rho}\right) = -\frac{\nabla \cdot \mathbf{u}^*}{\Delta t} \tag{2.9}$$

which is used to find the pressure field. Next, $\mathbf{u}^*$ is corrected by this pressure field and the updated solution $\mathbf{u}^{n+1}$ is found from Eq. (2.7).

We use a fixed Cartesian mesh of rectangular cells having sizes Δr for the radial direction, Δx for the vertical direction, as illustrated in figure 2. The spatial discretization of the variables u, v and p is based on the MAC method. The pressure and viscous terms in the momentum equations are calculated using second order central finite differences. In a MAC mesh, the variables are not defined on the same location, and the advantage is that in the solution of the resulting discretized Poisson equation, there is no checkerboard oscillation. The boundary condition for the pressure at the walls is the Neumann condition, corresponding to non-penetration, or zero normal velocity.

As pointed out in Li *et al.* (1998), the solution of the discrete counterpart of Poisson's equation (2.9) is the most time-consuming part of our Navier-Stokes solver and, consequently, an efficient solution is crucial for the performance of the whole method. The

multigrid method is used. The timings for each component of the code are detailed in
Renardy & Li (2000).

Finally, the CSF technique (Brackbill *et al.* (1992)) for the treatment of interfacial
tension is used. This component is described in detail in Renardy *et al.* (2000); Gueyffier
(2000).

The no slip boundary condition for the velocities is imposed at the walls. The boundary
condition for the color function is that it is zero outside of the physical domain. This is
equivalent to making the wall non-wetting, and the contact angle is 0 or 180 deg. Initial
condition is that we have a spherical drop suspended at a distance above the ground. We
impose an initial velocity in the downward direction on the viscous drop.

2.2. *The Marker Code: A Front-Tracking Algorithm*

The marker method of Duchemin *et al.* (2001); Popinet (2000); Popinet & Zaleski (1999,
2001) for free surface flows is used; the reader is referred to these references for details.
In summary, the momentum equations are solved on a Cartesian fixed grid. For cells
which are not cut by the free surface, a classical finite volume scheme is applied and the
Poisson equation is solved using a multi-grid algorithm. For the cells at the free surface,
velocities are extrapolated in order to enable the computation of finite differences. The
surface tension term is computed using cubic spline curves. The markers are advected by
the interpolated velocity field calculated on the fixed grid.

The front-tracking component is summarized as follows. The interface is represented
using an ordered list of marker particles (x_i, y_i), $1 \leqslant i \leqslant N$. A list of connected poly-
nomials $(p_i^x(s), p_i^y(s))$ is constructed using the marker particles and gives a parametric
representation of the interface, with s an approximation of the arc-length. Both lists are
ordered and thus identify the topology of the interface.

2.2.1. *Advecting the points*

The first step in the algorithm is the advection of the marker particles. A bilinear inter-
polation of the velocity field is used. The marker particles are advected in a Lagrangian
manner with a first-order explicit scheme. Once the points have been advected, we need
to reconstruct the parametric representation of the interface.

2.2.2. *Constructing the polynomials*

Cubic splines are used; these are connected cubic polynomials with continuous first
and second derivatives. The connection conditions for the interpolating polynomials lead
to two pseudo tridiagonal systems $Ba = c$, one for each coordinate of the parametric
curve, where B is a N^2 matrix. The solution is reduced to the solution of two tridiagonal
systems which are easily solved. Thus, the construction of the interpolating prametric
spline curve from the set of points $(\mathbf{x_i})$ requires the solution of four tridiagonal systems
of size N^2. This can be done in $\mathcal{O}(N)$ operations. All the other operations of the marker
algorithm deal with local computations along the interface. They are thus also of order
N. The ratio of time spent in the marker algorithm and in the computations done on
the bulk of the fluid is of order $1/N$.

2.2.3. *Redistribution*

As the interface evolves, the markers drift along the interface following tangential
velocities and we may need more markers if the interface is stretched by the flow. We
then need to redistribute the markers in order to ensure a homogeneous distribution of
points along the interface. This is done at each time step. This is similar to the approach
of boundary integral codes that also use arclength parameterization, cubic splines and
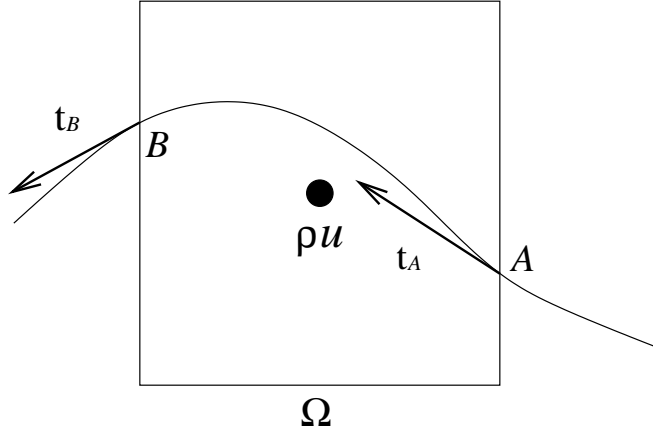redistribution of nodes

FIGURE 3. In the "method of tensions", the contribution of the surface tension to the momentum equation is obtained as the sum of two vectors tangent to the interface. First the direction of the vectors is determined from a spline representation of the interface, then the sum of the two tangent vectors times σ is added to the momentum balance of the cell.

2.2.4. *Surface tension contribution to the momentum equation*

The surface tension force is implemented as a traction in the direction tangential to the interface curve on the boundary of each control volume:

$$\sigma \oint_A^B \kappa \mathbf{n} ds = \sigma \oint_A^B d\mathbf{t} = \sigma(\mathbf{t_B} - \mathbf{T}_A), \tag{2.10}$$

where $\mathbf{t}$ is the oriented unit tangent to the curve. The control volume is shown in figure 3.

2.2.5. *Pressure gradient correction*

The method of Popinet & Zaleski (1999); Popinet (2000) takes account of the knowledge of the interface position and the fact that the pressure has a jump across the interface in order to adjust the finite difference expressions for pressure gradients at the interface.

3. Numerical results with the VOF method: SURFER++

Figure 4 is a schematic of the problem. We define a capillary number and Reynolds number

$$Ca = \frac{\eta V}{\gamma}, \qquad Re = \frac{VR\rho}{\eta}, \tag{3.1}$$

so that

$$We = Ca.Re, \qquad Oh = (\frac{Ca}{Re})^{1/2}. \tag{3.2}$$
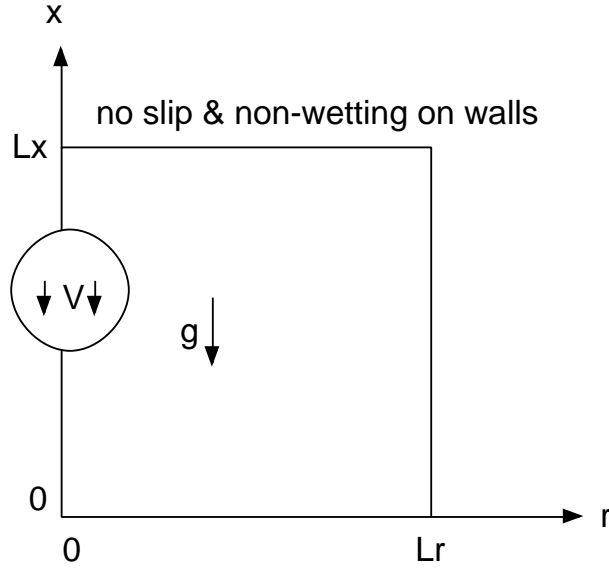
Y. Renardy et. al

FIGURE 4. Schematic of computational domain $[0, Lr] \times [0, Lx]$. The axisymmetric box is bounded by a wall which is non-wetting ($C = 0$ outside the physical domain), and on which there is no slip ($u = 0, v = 0$).

We choose the fluid parameters in our simulation so that the dimensionless parameters remain similar to those of figure 1. A limitation of SURFER++ is that the Ohnesorge number should not be smaller than 0.01. This limit gives $Ca/Re = 10^{-4}$. For $We = 4$, this yields $Re = 200, Ca = 0.02$. Thus, $We.Ca = 0.08$, which satisfies criterion (1.4). There is a trade-off in the simulations, that when the Ohnesorge number is larger with We fixed, Ca becomes larger, which increases $We.Ca$. We choose $\rho_{liq} = 1$, $\rho_{gas} = 0.012$, $R = 0.175$, $\gamma = 72.8$, $V = 40.8$, $\eta_{liq} = 0.0357$, $\eta_{gas} = 0.000642$, using cgs units, so that the ratios of densities and viscosities are $\rho_{liq}/\rho_{gas} = 83.3$, $\eta_{liq}/\eta_{gas} = 55.6$. Initially, the spherical drop is centered at height 0.25 cm. Timesteps in the explicit time integration scheme are $\Delta t = 5 \times 10^{-7}$. The computational domain is $[0, 0.45] \times [0, 0.45]$ and the mesh is 192×192.

Figure 5 shows the evolution for $t = 0$ to 0.01025s in steps of 0.00025s. Velocity vector plots are shown for $t = 0.005, 0.006, 0.007$s, in figure 7. A vortical motion is present at the step of the pyramid, both inside and outside the drop. The vortex outside the drop sits on the step. These features are coupled with the capillary waves.

The doughnut part of the drop has a toroidal vortex all around in the drop liquid. The impact velocity, when sufficiently high, pushes the center of the drop down, drying it out and leading to a singularity there. The evolution of kinetic energy is shown in figure 6. When the drop impacts the ground, the energy is dissipated through viscous effects, as well as through surface energy in the form of capillary waves. The capillary waves travel up the drop, forming the pyramid. They meet at the top of the pyramid, forming a nob. Thereafter, the center of the drop continues its descent downward. The simulation loses accuracy when the center of the drop dries and is stopped. At this point, the kinetic energy is at its minimum, and there is still some residual amount left, which is most apparent as the swirling motion in the bulk of the toroidal ring.

In figures 8-9, the simulation is started with the spherical drop touching the ground. This is because in the experiments, the superhydrophobic surface is highly corrugated,
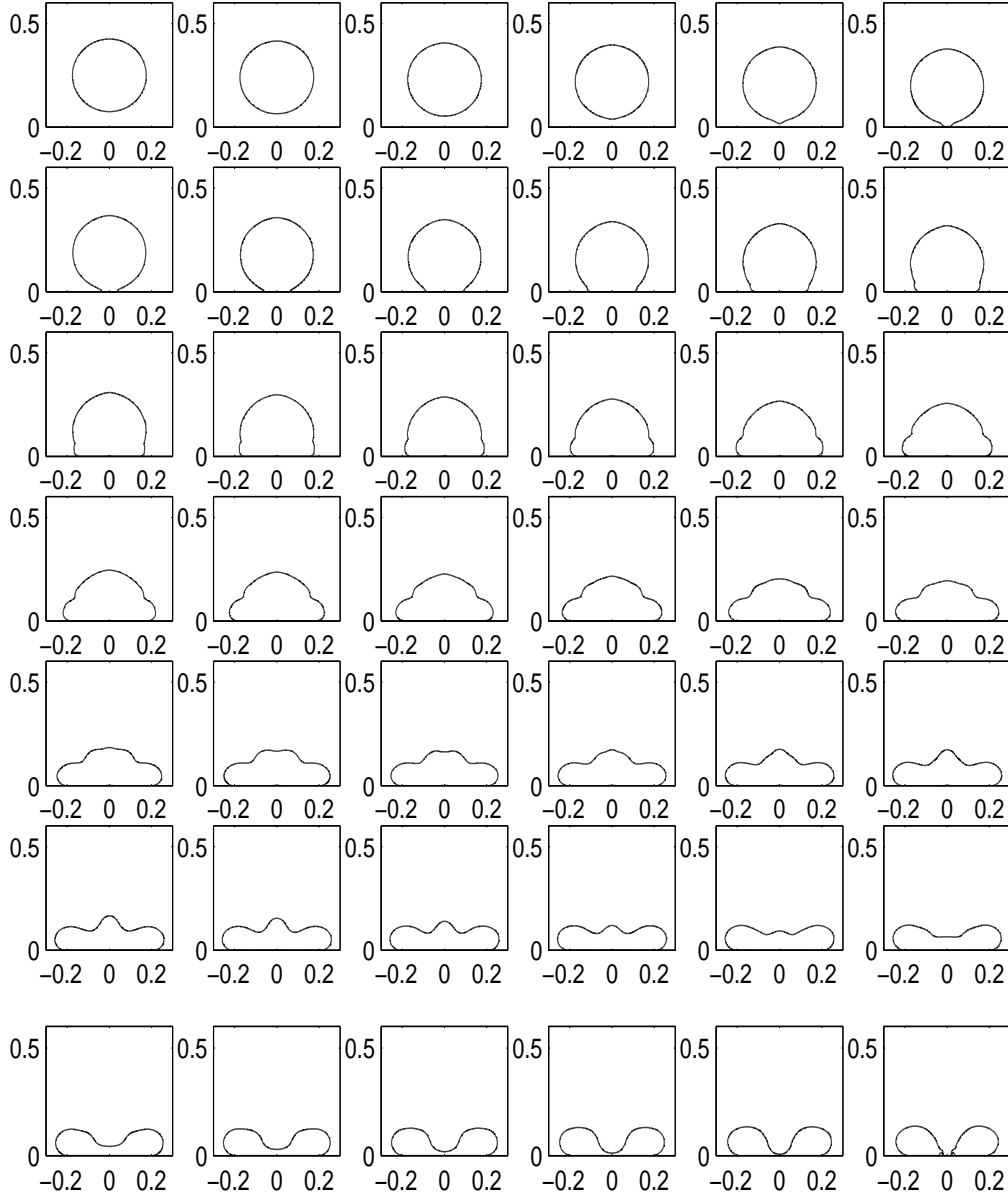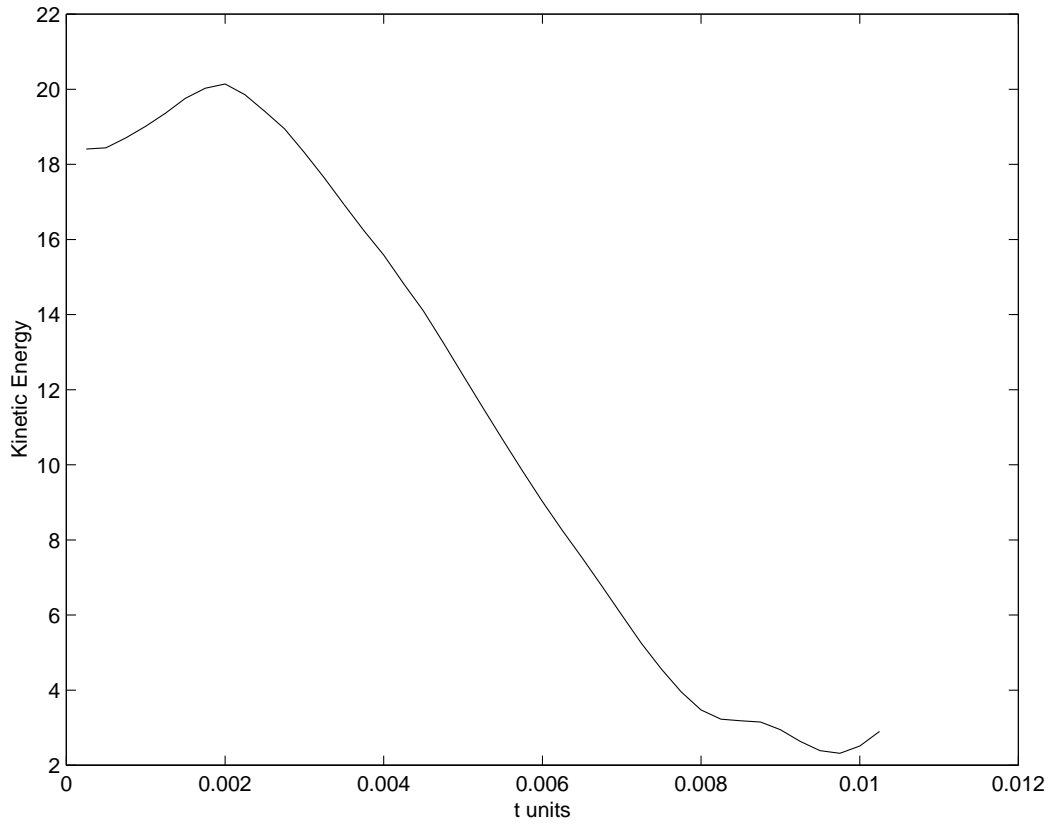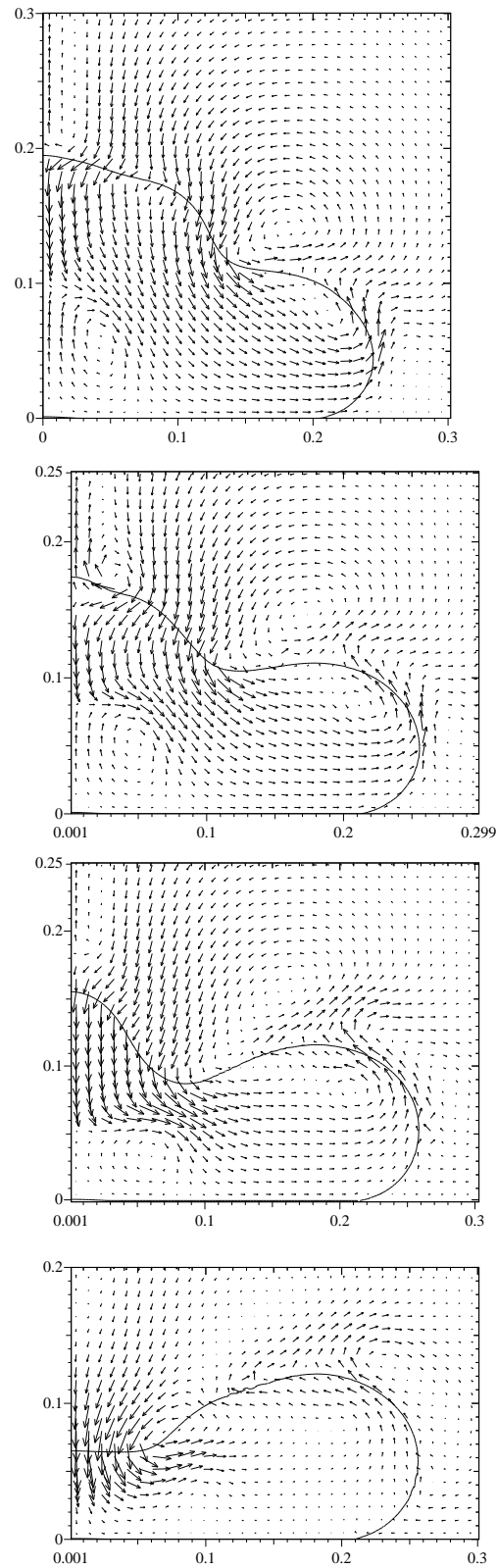
FIGURE 5. Impact of a drop of radius $R = 1.75$ mm at initial velocity $V = 40.8$ cm.s^{-1} starting at height 0.25 cm. The evolution across each row is from t=0 to 0.01025s in steps of 0.00025s. Mesh 192x192. Computational domain 0.45x0.45. Compare with figure 1.

and the air that is trapped due to the lubrication effect under the center of the drop as it descends to the ground can escape through the corrugation. However, in the numerical simulations, the lubrication layer persists so that the sides of the drop touch the ground first and the center of the drop elevates (Renardy *et al.* (2001)). The initialization of the drop to begin touching the ground at the center of the drop is therefore a closer approximation of what is happening in the experiments. Here, the impact velocity is slightly less than in the previous simulation and the drop does not dry out at the center.

FIGURE 6. Impact of a drop of radius $R = 1.75$ mm at initial velocity $V = 40.8$ cm.s^{-1} starting at height 0.25 cm. Kinetic energy evolution for figure 5.

Instead, it almost dries out, at the first minimum of the kinetic energy, also plotted in the figure. The drop then begins to rise at the center as the kinetic energy increases again. The kinetic energy then decreases as the amount of contact of the drop with the ground decreases and the drop eventually lifts up. This simulation is presented up to 0.0165s.

FIGURE 7. Impact of a drop of radius $R = 1.75$ mm at initial velocity $V = 40.8$ cm.s^{-1} starting at height 0.25 cm. Velocity vector plots at $t = 5 \times 10^{-3} + 1 \times 10^{-3}n$, $n = 0, 1, 2, 3$. Compare with figure 1.
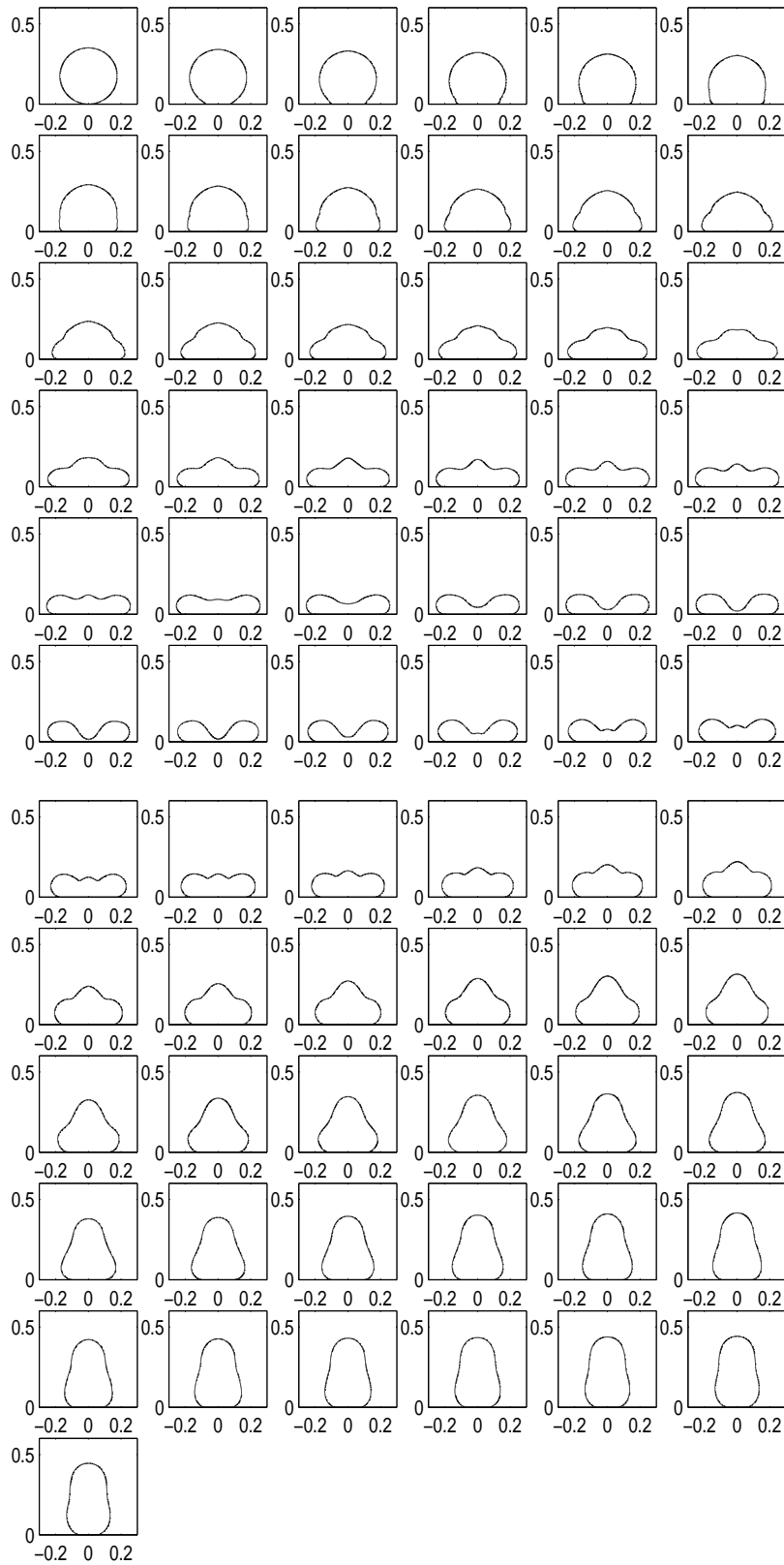
FIGURE 8. Impact of a drop of radius $R = 1.75$ mm at initial velocity $V = 40.8$ cm.s^{-1} starting touching the ground. The evolution proceeds across each row, from $t = 0$ to 0.00875 in steps of 0.00025s, then $t = 0.009$ to 0.0165s.
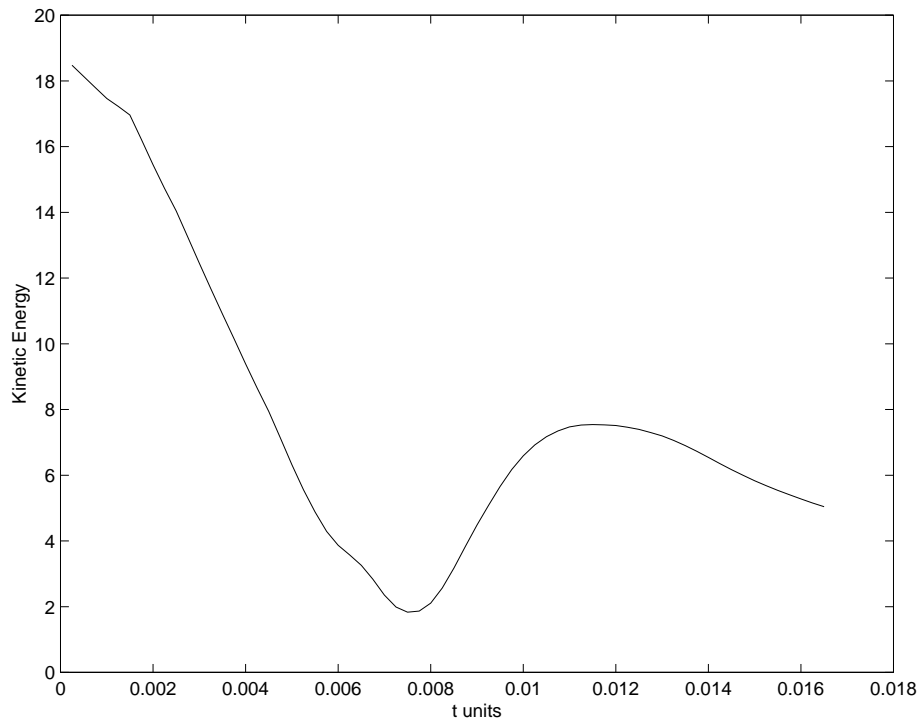
FIGURE 9. Impact of a drop of radius $R = 1.75$ mm at initial velocity $V = 40.8$ cm.s^{-1} starting touching the ground. Plot of kinetic energy evolution.

3.1. *Ellipsoidal initial shape*

Upon a re-examination of figure 1, it is evident that the initial shape of the drop just before impact with the ground is not spherical. It is ellipsoidal. This shape may be induced by vibrations upon drop production. The radii which model the experimental photographs are $R_{\mathrm{horizontal}} = 0.15$ and $R_x = 0.24$cm. The viscosities are scaled up by factor 3 to 0.000642 and 0.0357, keeping the true viscosity ratio between water and air. The densities are 0.012 and 1.0. The drop is initially touching the ground. The computational box is [0,0.45]cm × [0,0.675]cm.

3.1.1. *Impact velocity $V = 40.8\,cm.s^{-1}$*

The initial velocity is $V = 40.8$ cm.s^{-1}. This computation is performed on a mesh of 256x384. Figure 10 shows the evolution of the interface shape until the center of the drop dries out. In comparison with the simulation for a spherical drop, the ellipsoidal drop develops more of the pyramid shape, together with the nob at the center which rises up as in the experiments. Figure 11 shows velocity vector plots for situations which mirror the experimental photographs of figure 1.

A convergence test for spatial refinement is shown in figure 12 for the evolution of kinetic energy, for meshes 256x512, 384x576, and 512x768. We see that the 256x512 case gives a qualitatively good estimate of the more refined cases. A comparison of interfacial shapes was conducted; the main improvement in mesh refinement occurred in the resolution of the nob at the top of the pyramid, but the refinement did not show new essential features. The CPU time required for the 512x768 case on the Origin 2200 is roughly 4 hours per 50 timesteps, with $\Delta t = 0.5 \times 10^{-6}$s. The CPU time for the 384x576 case is roughly 1 hour 15 minutes for the 50 timesteps at the same Δt. The kinetic energy reaches its minimum when the center of the drop dries out. The velocity field in figure 11 shows that there is a small amount of kinetic energy stored in the drop as motion inside the toroidal region.
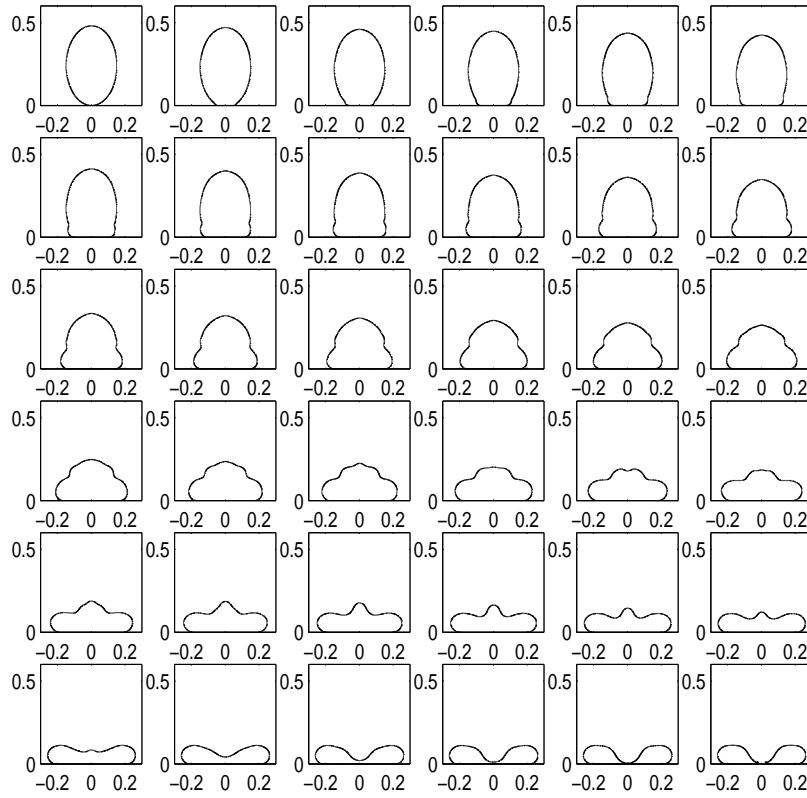
FIGURE 10. Impact of an ellipsoidal drop of radius $R_{\mathrm{horiz}} = 1.5$, $R_x = 2.4$ mm at initial velocity $V = 40.8$ cm.s^{-1} started touching the ground. Progression across each row at every 0.00025s up to 0.00875s. 384x576 mesh.
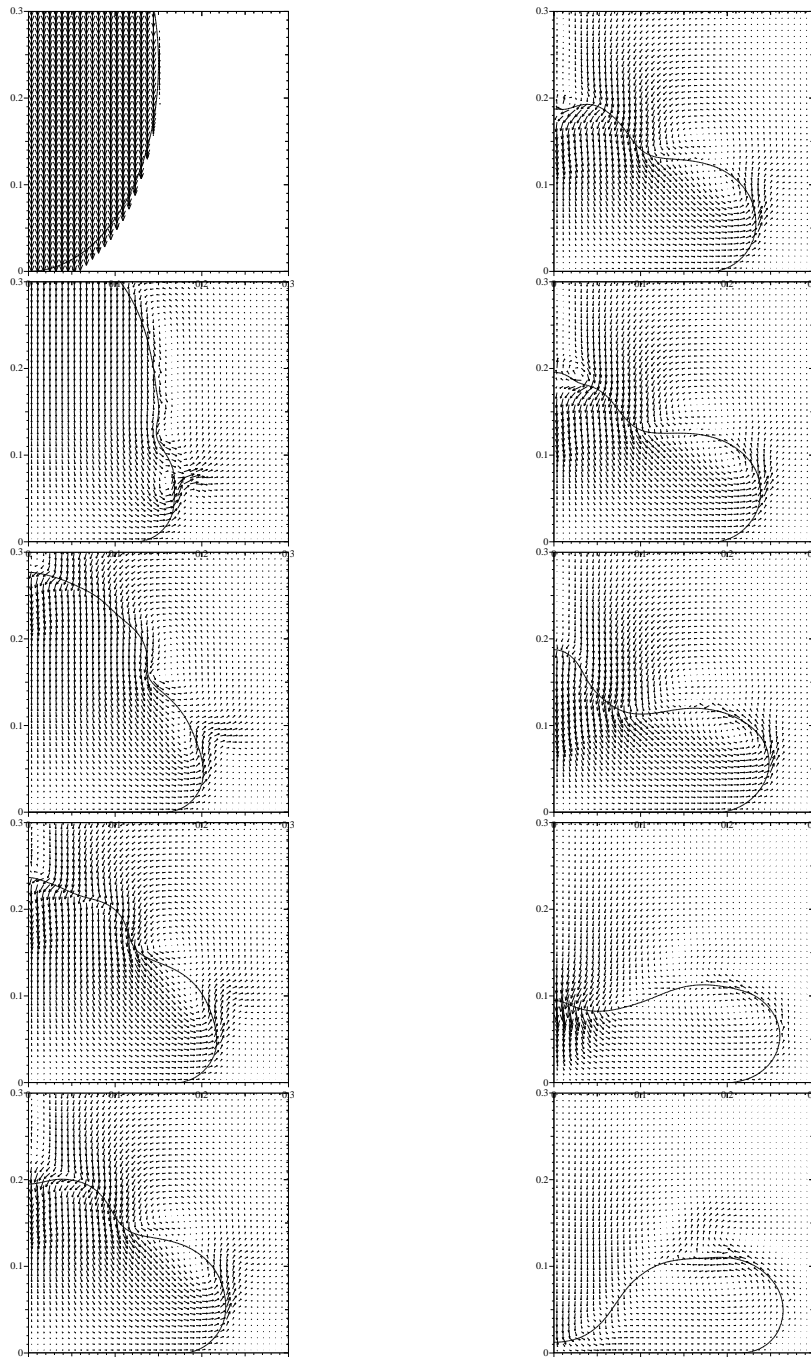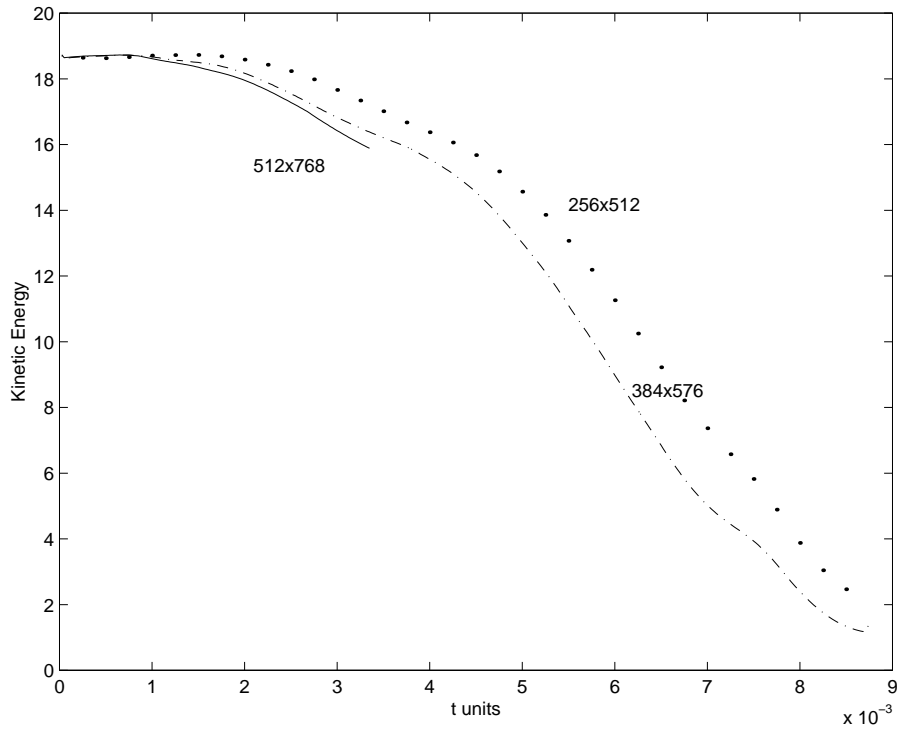
FIGURE 11. Impact of an ellipsoidal drop of radii $R_{\mathrm{horiz}} = 0.15$, $R_x = 0.24$cm at initial velocity $V = 40.8$ cm.s^{-1} started touching the ground. t=(1, 11,17, 20, 22, 23, 24, 26,30,34) $\times 0.00025s$. Compare with figure 1.

FIGURE 12. Impact of an ellipsoidal drop of radii $R_{\mathrm{horiz}} = 0.15, R_x = 0.24$cm at initial velocity $V = 40.8$ cm.s^{-1} started touching the ground. Kinetic energy vs time, computed in $[0, 0.45] \times [0, 0.675]$ with different meshes: $\Delta r = \Delta x = 0.45/512$ (-), $0.45/384$ (-.-), $0.45/256$ (..).

3.1.2. *Initial velocity $V = 38\,cm.s^{-1}$*

The next simulation is conducted at a slightly lower impact speed, 38 cm.s^{-1}. Figure 13 shows velocity vector plots for situations which are close to the stages photographed in figure 1. The kinetic energy evolution is shown in figure 14, and the last plot of figure 13 is close to the first minimum of the kinetic energy. Here, the center of the drop is thin. The situation at the minimum is shown in figure 15, where velocity vector plots for the drop as the kinetic energy evolves further are shown.

At this impact speed, the center of the drop does not dry out, and the drop partially rebounds, as shown in figures 15 and 16. When the center of the drop begins its rise from its minimum height, the kinetic energy increases to its local maximum. This stage is shown in figure 15(c). Thereafter, as the drop begins to lift off the ground, as in figure 15(d), the kinetic energy decreases again.

At the stage of evolution shown in figure 16, the velocities are small relative to the initial stages, and we choose to display just the interface shapes. After the drop lifts off the ground, the drop evolves to a top-heavy champignon-like shape, and then to a flatter shape with a dimple at the bottom. The drop hovers in response to the lubrication layer created at the top wall. It approaches the top wall closer to the rim rather than the center. This is typical of a drop approaching a solid; see for instance the two-dimensional simulations of a drop falling to the ground in Renardy *et al.* (2001).
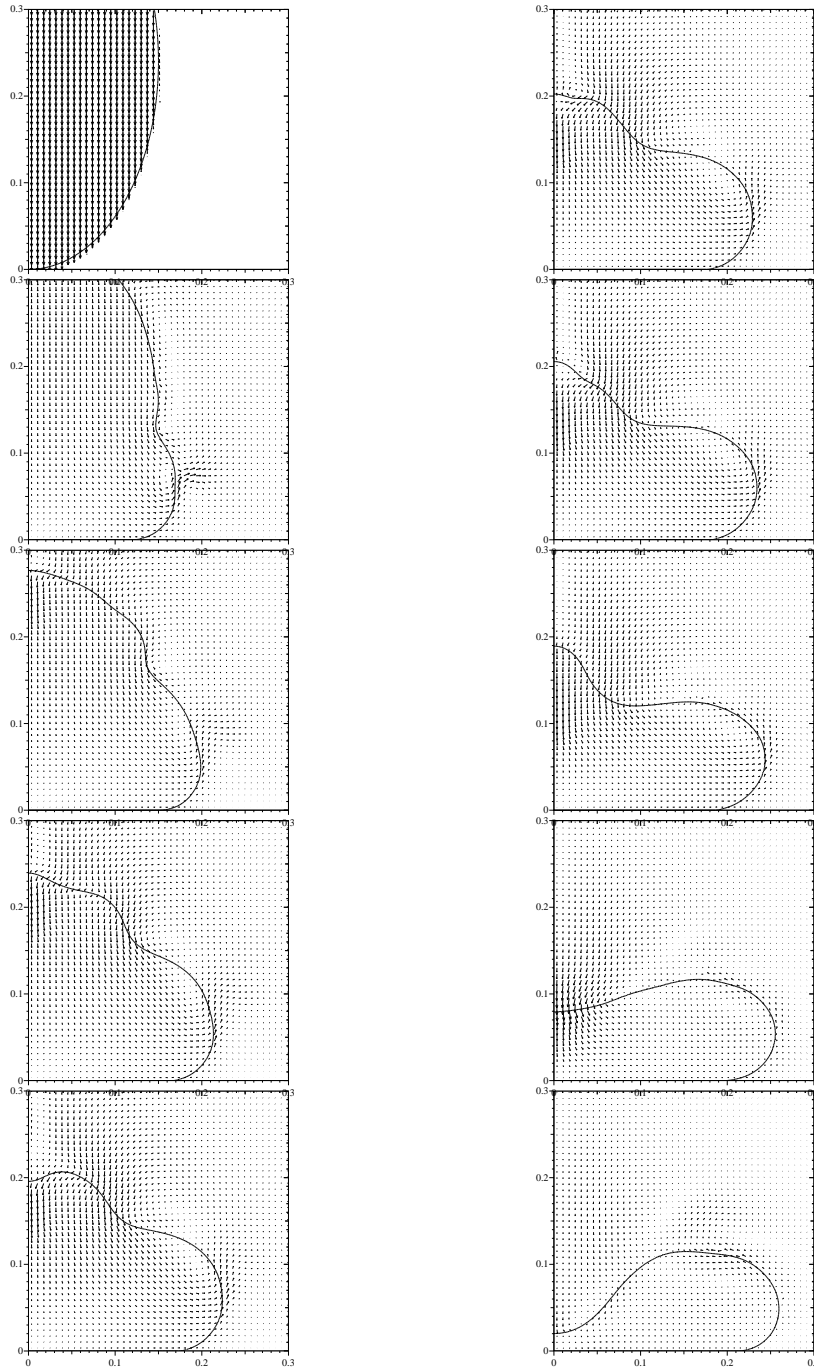
FIGURE 13. Impact of an ellipsoidal drop of radii $R_{\mathrm{horiz}} = 0.15$, $R_x = 0.24$cm at initial velocity $V = 38$ cm.s^{-1} started touching the ground. t=0.00005, (11,17, 20, 22, 23, 24, 26,30,34) $\times 0.00025 s$. Compare with figure 1.
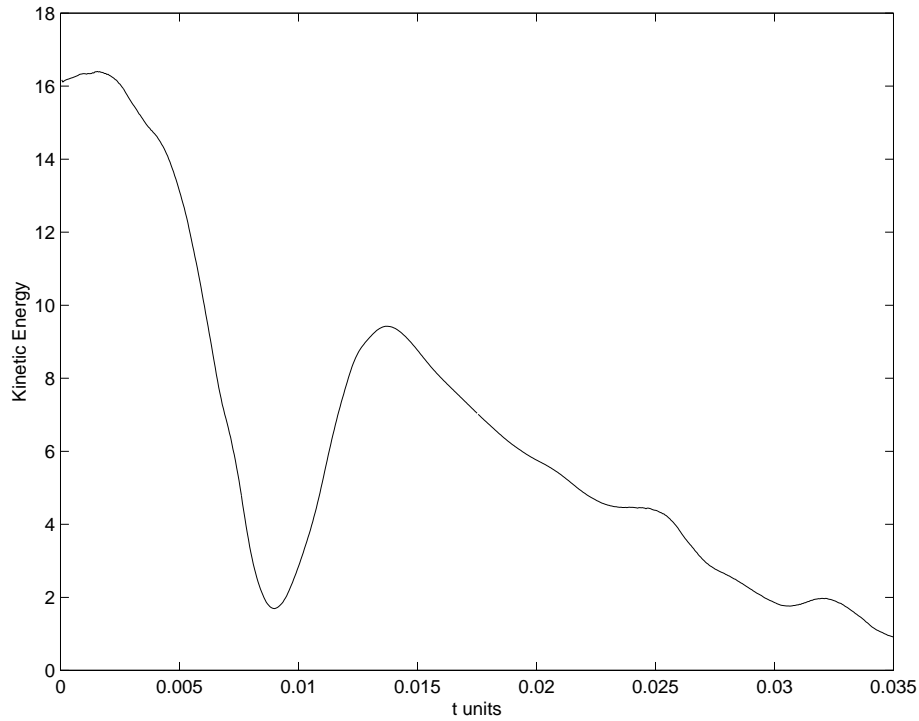
Y. Renardy et. al

FIGURE 14. Impact of an ellipsoidal drop of radii $R_{\mathrm{horiz}} = 0.15, R_x = 0.24$cm at initial velocity $V = 38$ cm.s^{-1} started touching the ground. Kinetic energy vs time, computed in $[0, 0.45] \times [0, 0.675]$ with mesh $\Delta r = \Delta x = 0.45/256$.
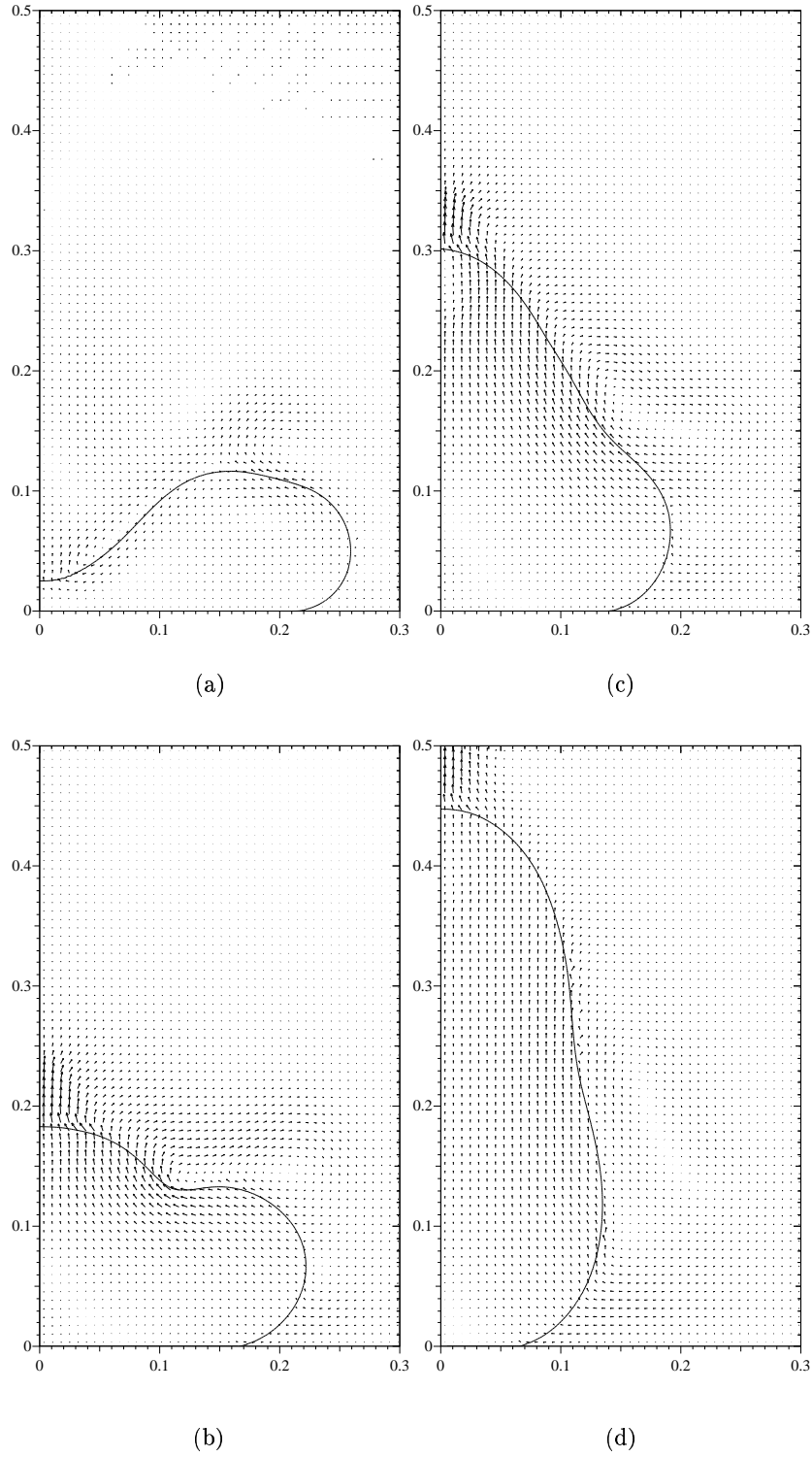
FIGURE 15. Impact of an ellipsoidal drop of radii $R_{\mathrm{horiz}} = 0.15$, $R_x = 0.24$cm at initial velocity $V = 38$ cm.s^{-1} started touching the ground. t= (a) 0.009 (minimum kinetic energy 1.69), (b) 0.012, (c) 0.0137 (local maximum kinetic energy 9.4), (d) 0.0175s.
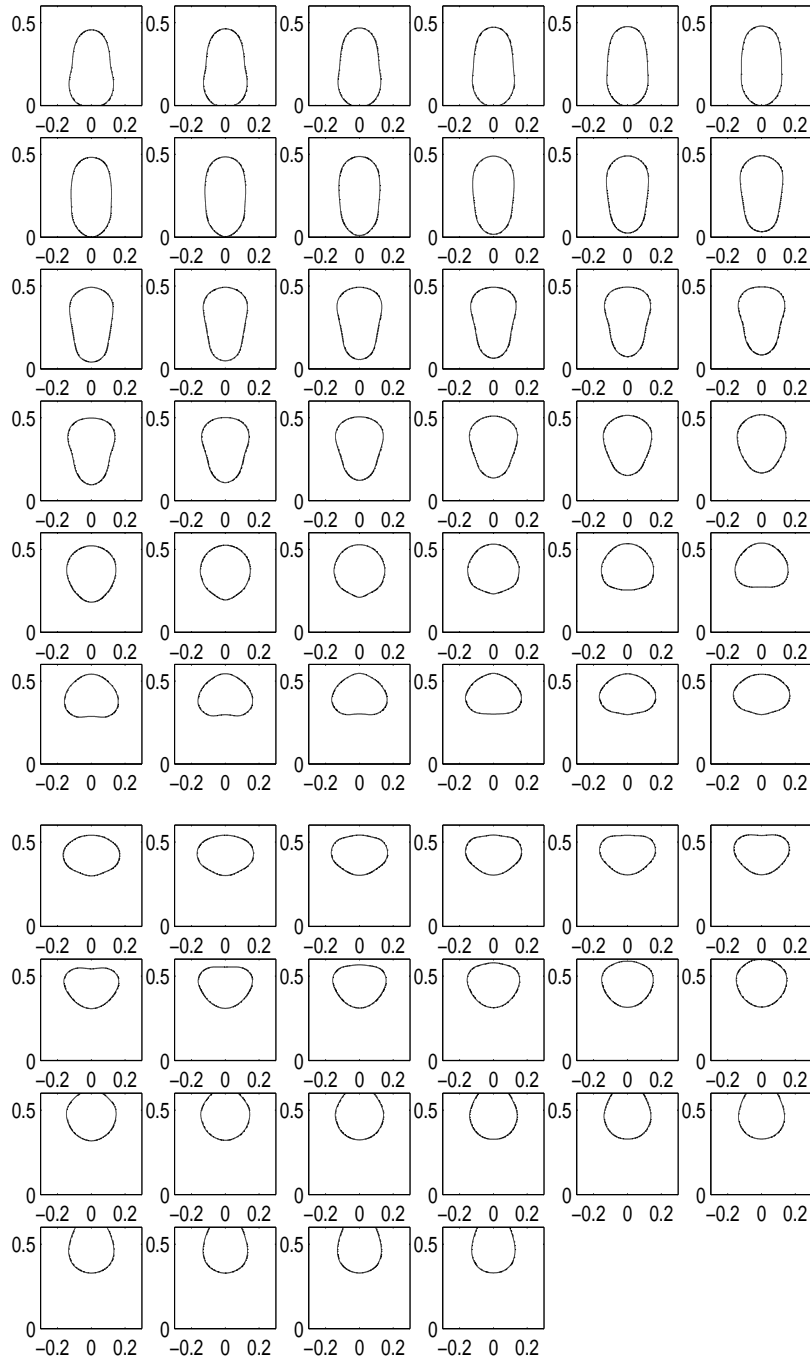
FIGURE 16. Impact of an ellipsoidal drop of radii $R_{\mathrm{horiz}} = 0.15$, $R_x = 0.24$cm at initial velocity $V = 38$ cm.s^{-1} started touching the ground. t=0.0178 to 0.0349s, going across, in steps of 0.0003s.
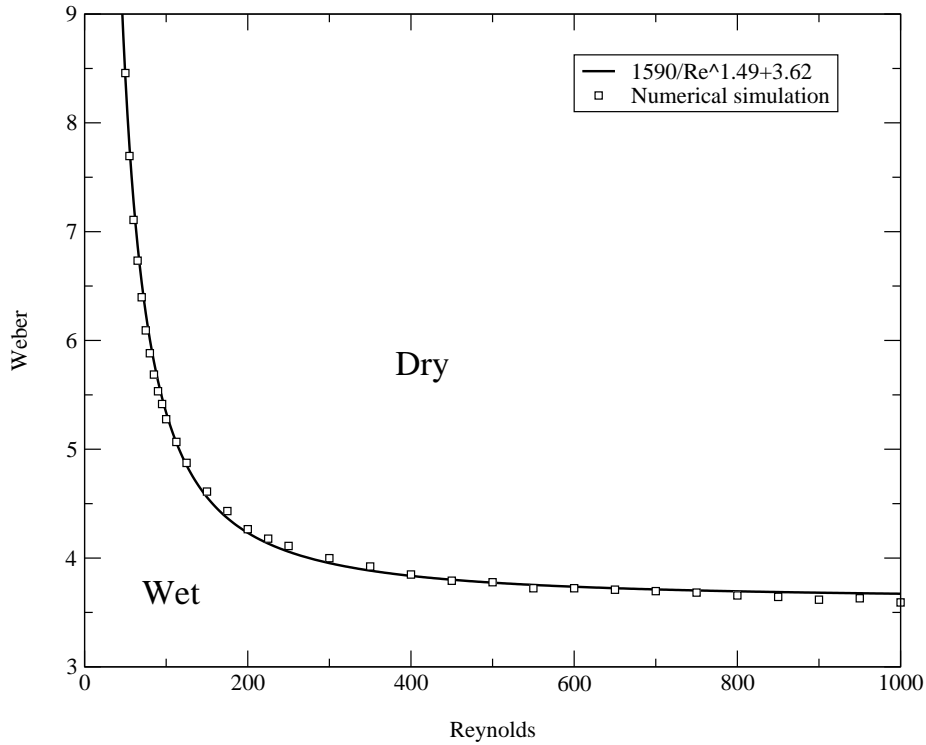
FIGURE 17. Universal curve delineating conditions for dryout. Initial drop is spherical.

4. Numerical simulations with the Marker Method

The simulations are conducted in a computational box 14/3 mm square with a 256x256 grid. A spatial refinement study was conducted with 512x512 to check for convergence. The density of the liquid is 1 gm.cm^{-3}, and the viscosity is 1 cP. The surface tension is 72.8 dyn.cm^{-1}. The drop is initially centered at 2.193 mm above the ground.

4.1. *Universal curve for dryout*

Figure 17 describes the critical values of Weber and Reynolds for which the drop becomes a torus after impact. The initial drop is spherical. The intersection of the bottom wall with the axis of symmetry is "Wet" for a spherical topology and "Dry" for a toroidal one. The formula shown in the figure for the curve is an empirical fit.

At high Reynolds numbers, viscous effects are small and the topology is determined by a competition between inertia and surface tension alone. Thus, the Weber number becomes the only dimensionless parameter and the graph asymptotes to We =constant, independent of the Reynolds number. On the other hand, at low Reynolds numbers, viscous effects are important and, therefore, a combination of both We and Re determines the critical curve.

Given an experimental set-up, figure 17 guides the selection of the drop velocity to achieve the desired condition. For example, in the development of technology for liquid-metal microdroplet deposition (Fukai *et al.* (1995)), the "wet" condition is desired.

4.2. *Initially oscillating drop*

We begin by showing in figure 18 the corresponding simulation for the experimental results of figure 1 displayed in Section 1: 2.7 ms (between photo 1 & 2), 1.8 (between 2 & 3, and so on), 0.4, 1.0, 0.2, 0.2, 0.4, 0.4, and 0.9. The initial drop is well-approximated by a mode of oscillation of a drop released from a nozzle, namely mode 2; the distance from the center of the drop to the free surface is:

$$r(\theta) = R_0(1.0 + \epsilon Y_2(\theta)) \tag{4.1}$$

where $Y_2(\theta)$ is a spherical harmonic of order 2 (Lamb (1932); Plesset & Prosperetti (1977)). These are linear modes of oscillation so that the application of this for $\epsilon = 0.29$ deviation is an estimate of the initial shape, in the same spirit as the ellipsoidal initial drop. Although we acknowledge that the initial shape of the drop may be due to the mode 2 oscillation, we do not attempt to include the velocity of the oscillations in our computations, because we do not know at what phase of the oscillation the drop is at impact. If the drop is at maximum distortion, the velocity is zero in the linear approximation. We can estimate the order of magnitude of the velocity of the oscillations. According to Lamb (1932), the frequency for a water drop is

$$\omega = 24.3a^{-3/2}, \tag{4.2}$$

where a is the radius of the drop (all numbers are in CGS units). For a maximum radial distortion of ϵa, we therefore find a maximum speed of

$$u_m = 24.3\epsilon a^{-1/2}. \tag{4.3}$$

With $\epsilon = 0.29$ and $a = 0.175$, this yields $u_m = 16.85$. This speed, however, would be attained at the time when the distortion is zero and the drop is spherical. We believe that the drop at impact is actually close to maximum distortion and, therefore, the speed due to the oscillation at the time of impact is small relative to the impact speed. The period of the oscillation is

$$T = 2\pi/\omega = 0.019 \text{ seconds}, \tag{4.4}$$

which is much longer than the duration of the impact.

Our numerical results, shown in virtual reality in figure 18, succeeds in capturing the gross features of figure 1. We have conducted a spatial convergence test for these results and show in figure 19 the interface positions through a cross-section for the 256x256 case and the refined 512x512 case. These show that the 256x256 result captures the qualitative features, while the 512x512 case accentuates the small capillary wave at the top. In summary, the results of the free-surface marker code compare well with those of the two-fluid volume-of-fluid code, and with the experiments of Richard (2000).

Figure 20 shows the contours for the pressure field corresponding to four of the stages presented in figure 18. These show contour lines given at regular spacings of the pressure values. Clearly, the maximum values evolve toward the top of the pyramid.

5. Conclusions

When a drop of liquid impacts a hydrophobic surface, it evolves to a pyramid structure when the impact speed is sufficiently high and capillary waves persist over the surface of the impacting drop. In terms of dimensionless parameters, this criterion requires the Weber number $We > 1$ and the product of the Weber and capillary numbers $We.Ca < 1$.

Numerical simulations are conducted for a drop of clean water, with two different

algorithms. One is the two-fluid volume-of-fluid method, in which the true viscosity ratio of air to water has been used, while upscaling the values of each viscosity by factor 3, and the gas density has been upscaled by factor 10. The second method is the free-surface front-tracking algorithm. Both methods show qualitatively similar results for the drop evolution, and a satisfactory comparison with the experimental photographs is achieved.

We resolve the open question which was presented in Richard (2000), namely the maximal radius was estimated by balancing with the initial kinetic energy, and the experimental data showed it to be less than the predicted value. In this paper, the kinetic energy evolution is tracked numerically, together with the velocity and pressure fields, and interface position. We find that at the first minimum value of kinetic energy, the drop achieves its maximal spreading radius and is toroidal, storing the remaining kinetic energy in a swirling motion in the drop. This is followed by a rebound of the drop when the impact speed is sufficiently high, but the kinetic energy on the rebound is a fraction of the original value. The energy is also diverted to deform the surface through capillary waves, and there is also viscous dissipation.

We have also determined the universal curve in the Reynolds number vs Weber number space for the conditions under which the center of the drop dries out. In a given experiment where the impact speed can be varied, this study shows that there is a critical impact speed beyond which the center dries out.

We comment that the fine structure of the capillary waves may well be affected by small changes in the initial condition. It is likely that not only the drop ellipticity, but the velocity field inside would play a role. For instance, when one does a study of a plane capillary wave oscillation or an instability, it is very important to initiate not only the interface deformation but also the velocity field. In addition to the velocity field coming from the possible oscillations of the drop upon its creation, there may be a contribution from air friction during the fall. Furthermore, the droplet is in a state of superposition between various modes of oscillation, as not only mode 2 is excited. While a numerical study of these issues is worthwhile, it is premature before extensive experimental data concerning the drop before impact is available. One aim of this paper is to promote such a call for experiments.
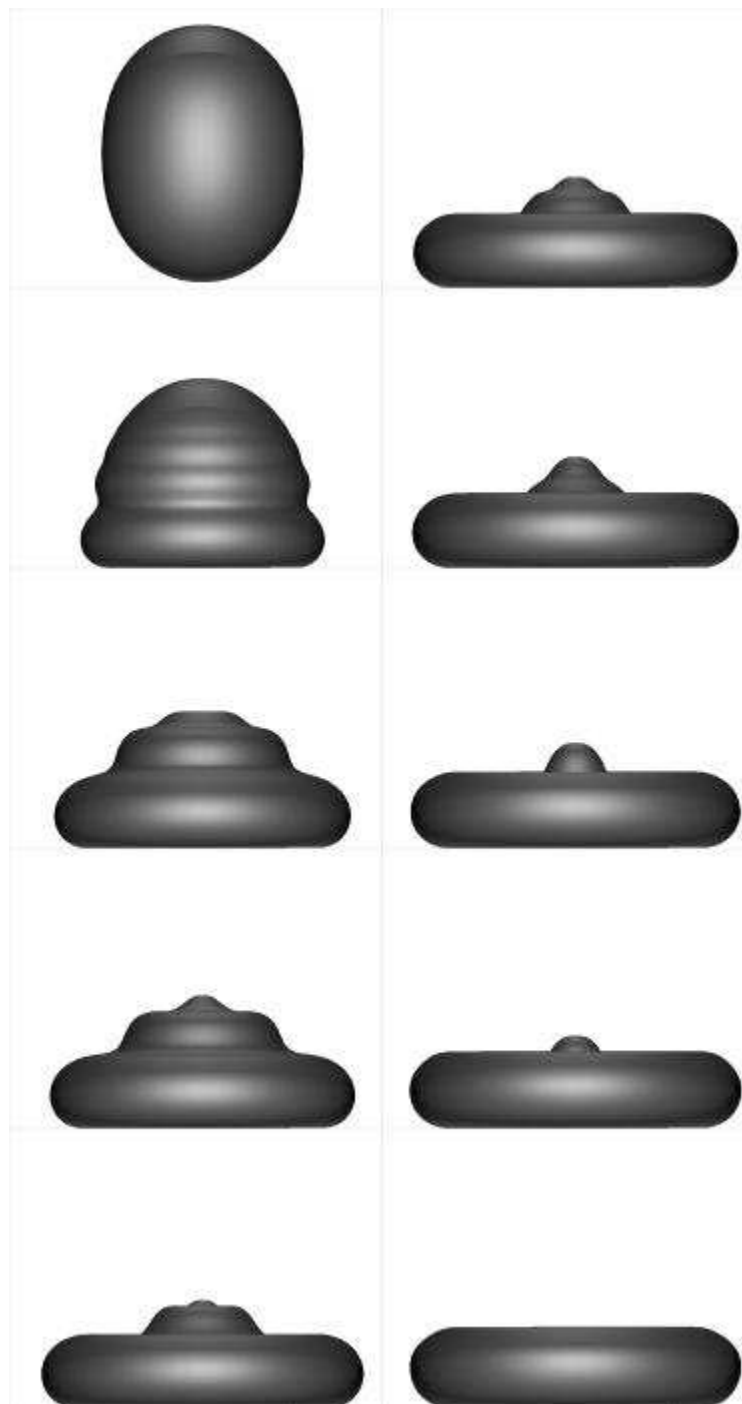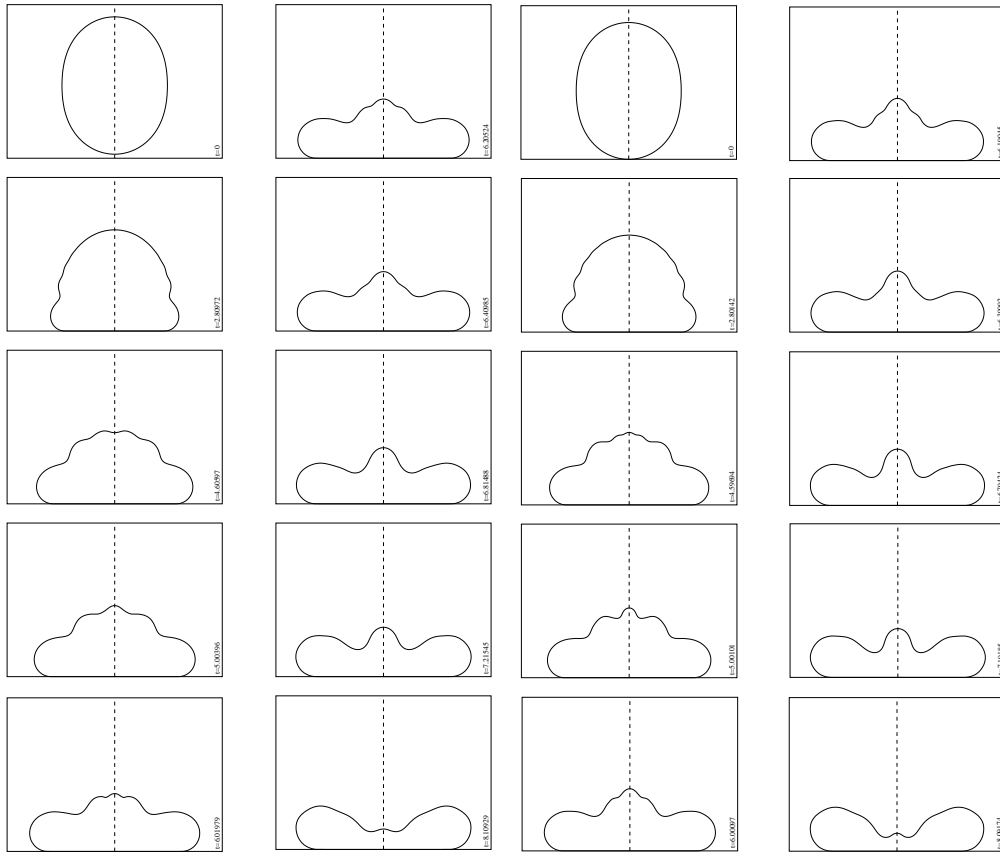
Y. Renardy et. al

FIGURE 18. Simulations with the Marker Code. Initial drop is mode 2, with $R_0 = 1.75$mm and $\epsilon = 0.29$ in Equation (4.1). Timings between frames are the same as those of the experiment in figure 1.

(a)   (b)

FIGURE 19. Initial drop is mode 2, with $R_0 = 1.75$mm and $\epsilon = 0.29$ in Equation (4.1). Timings between frames are the same as those of the experiment in figure 1. Spatial convergence test for (a) 256x256 and (b) 512x512 cases.
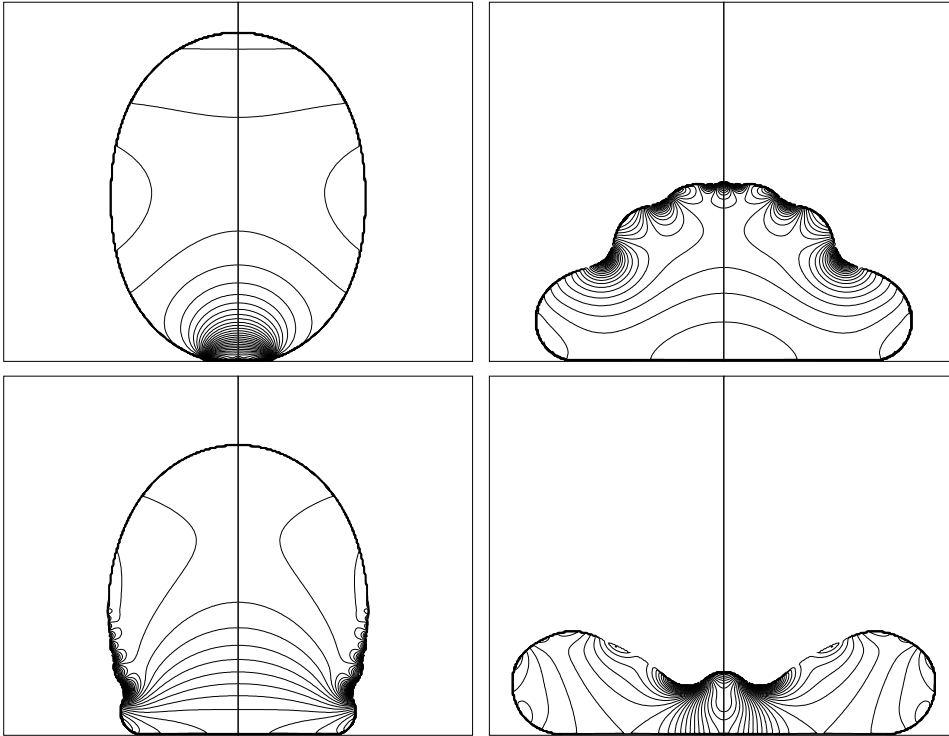
FIGURE 20. Simulations with the Marker Code. Initial drop is mode 2, with $R_0 = 1.75$mm and $\epsilon = 0.29$ in Equation (4.1). Pressure fields are shown corresponding to the drop evolution of figure 18.

REFERENCES

BOULTON-STONE, J. M. & BLAKE, J. R. 1993 Gas bubbles bursting at a free surface. *J. Fluid Mech.* **254**, 437–466.

BRACKBILL, J. U., KOTHE, D. B. & ZEMACH, C. 1992 A continuum method for modeling surface tension. *J. Comp. Phys.* **100**, 335–354.

DUCHEMIN, L., POPINET, S. & ZALESKI, S. 2001 Jet formation in bubbles bursting at a free surface. *preprint* -, –.

FUKAI, J., SHIBA, Y., YAMAMOTO, T., MIYATAKE, O., POULIKAKOS, D., MEGARIDIS, C. M. & ZHAO, Z. 1995 Wetting effects on the spreading of a liquid droplet colliding with a flat surface: experiment and modeling. *Phys. Fluids* **7/2**, 236–247.

GUEYFFIER, D. 2000 Etude de l'impact de gouttes sur un film liquide mince. PhD thesis, Université Pierre et Marie Curie.

GUEYFFIER, D., LI, J., NADIM, A., SCARDOVELLI, R. & ZALESKI, S. 1999 Volume-of-fluid interface tracking and smoothed surface stress methods for three-dimensional flows. *J. Comp. Phys.* **152**, 423–456.

LAFAURIE, B., NARDONE, C., SCARDOVELLI, R., ZALESKI, S. & ZANETTI, G. 1994 Modelling merging and fragmentation in multiphase flows with SURFER. *J. Comp. Phys.* **113**, 134–147.

LAMB, H. 1932 *Hydrodynamics*. Cambridge University Press.

LI, J. & RENARDY, Y. 2000 Numerical study of flows of two immiscible liquids at low Reynolds number. *SIAM Review* **42**, 417 – 439.

LI, J., RENARDY, Y. & RENARDY, M. 1998 A numerical study of periodic disturbances on two-layer Couette flow. *Phys. Fluids* **10**, 3056–3071.

OGUZ, H. N. 1998 The role of surface disturbances on the entrainment of bubbles. *J. Fluid Mech.* **372**, 189–212.

PLESSET, M. S. & PROSPERETTI, A. 1977 Bubble dynamics and cavitation. *Ann. Rev. Fluid Mech.* **9**, 145–185.

POPINET, S. 2000 Stabilité et formation de jets dans les bulles cavitantes: Développement d'une méthode de chaîne de marqueurs adaptée au traitement numérique des équations de navier-stokes avec surfaces libres. PhD thesis, Université Pierre et Marie Curie.

POPINET, S. & ZALESKI, S. 1999 A front-tracking algorithm for the accurate representation of surface tension. *Int. J. Numer. Methods Fluids* **30(6)**, 775–793.

POPINET, S. & ZALESKI, S. 2001 Bubble collapse near a solid boundary: a numerical study of the influence of viscosity. - -, submitted.

QUÉRÉ, D., BICO, J. & RICHARD, D. 2000 Three attempts on dry wetting. *Nonlinear waves in multi-phase flow* **ISBN 0-7923-6454-6 Kluwer Academic Publishers**, 195–203.

RENARDY, M., RENARDY, Y. & LI, J. 2001 Numerical simulation of moving contact line problems using a volume-of-fluid method. *J. Comp. Phys.* **to appear**, –.

RENARDY, Y. & LI, J. 2000 Parallelized simulations of two-fluid dispersions. *SIAM News* **in 'Applications on Advanced Architecture Computers', G. Astfalk ed.**, December, 1.

RENARDY, Y. & LI, J. 2001 Merging of drops to form bamboo waves. *Int. J. Multiph. Flow* p. In press.

RENARDY, Y., RENARDY, M. & CRISTINI, V. 2000 A new volume-of-fluid formulation for surfactants and simulations of drop deformation under shear at a low viscosity ratio. *Eur. J. Mech. B/ Fluids* **submitted**.

RICHARD, D. 2000 Situations de mouillage nul. PhD thesis, Université Paris VI.

RICHARD, D. & QUÉRÉ, D. 2000 Bouncing water drops. *Europhys. Lett.* **50(6)**, 769 – 775.

ZALESKI, S., LI, J., SCARDOVELLI, R. & ZANETTI, G. 1995 Flows with interfaces: dealing

with surface tension and reconnection. In *Proceedings of the IMACS-COST Conference on Computational Fluid Dynamics,conference, Lausanne Sept. 13-15, 1995,Notes on Numerical Fluid Mechanics*. Vieweg, 53.